Image Reconstruction: Off-Resonance Effects and Correction

Brad Sutton
Bioengineering Department
**University of Illinois at Urbana-Champaign**

1. INTRODUCTION

When put into the magnetic field, a tiny but detectable fraction of the protons present in water in the body will align with this strong, steady magnetic field. During imaging, the tissue of interest is occasionally subjected to a brief electromagnetic radio-frequency (RF) pulse, essentially tilting the aligned protons off the axis of the main magnetic field. The protons then precess around the main field axis at a known frequency proportional to the main magnetic field. That field can be manipulated to identify the location of certain types of activity. The rate of precession can be used, for example, to encode the spatial position of the protons for imaging, by creating a gradient in the magnetic field along one direction [1]. The protons then precess at different frequencies depending on their location, as the magnetic field that they experience is due to both the main magnetic field and the applied imaging gradient. Signal intensity and spatial localization in MRI rely on a uniform magnetic field existing throughout the sample of interest. Much effort is devoted to properly designing and shimming the main magnetic field to achieve uniform intensity.

However, these efforts to create a uniform magnetic field are limited by the fact that different tissues and materials possess a property called magnetic susceptibility, a property that reflects the magnetizability of a substance. This magnetic susceptibility, denoted by χ, affects the magnetic field that protons experience inside that tissue or material. Different tissues and air spaces in the body possess different magnetic susceptibility, which can lead to artifacts during imaging. Since this effect disrupts the uniformity of the magnetic field, it is referred to as magnetic field inhomogeneity or bulk magnetic susceptibility (BMS). In the brain, the magnetic susceptibility differences between soft tissues ($\chi = -9 \times 10^{-6}$) and air ($\chi = 0.4 \times 10^{-6}$) result in field inhomogeneity, especially at regions around air/tissue interfaces [2]. Therefore, certain regions in the brain are particularly problematic to image, including the orbitofrontal cortex and amygdala, which are of very considerable interest in functional MRI for cognitive, affective, and clinical psychophysiology.

Figure 1 provides an example of the image distortions and signal loss that result from air/tissue magnetic susceptibility differences in fMRI images, which are weighted to reflect susceptibility differences in blood for the BOLD contrast. Many of the imaging artifacts that will be discussed are present in all types of imaging, to some extent. However, due to the desired susceptibility weighting in functional MRI, we will discuss field inhomogeneity effects with respect to the fMRI application. Generally, fMRI images are collected as gradient echo images with fairly <u>long echo times</u> (25-40 ms) and as single-shot acquisitions with <u>long data acquisition</u> windows. These properties contribute to susceptibility-induced <u>signal loss</u> and geometric <u>image distortions</u>, respectively. Susceptibility-induced signal loss is a function of the magnetic field gradients through a voxel and increases with slice thickness and echo time in gradient echo acquisitions. In Figure 1, note the dramatic signal loss in lower-right portion of panel (d). BMS-induced image distortions are a function of phase accumulations during the data acquisition readouts and increase with increasing data acquisition times and decreasing bandwidth of the readout. Even though spin echo acquisitions do not suffer from susceptibility-induced signal losses, they still display similar levels of BMS-induced distortions. This is critical for diffusion weighted imaging and other structural acquisitions that use long data readouts, including single-shot acquisitions.

In the sections that follow, we consider these two susceptibility effects and mechanisms to correct them.

Figure 1: Two types of image artifact resulting from bulk magnetic susceptibility differences near air/tissue interfaces in the brain. An EPI simulation based on a measured image and field map is shown in (a-c): (a) reference image, (b) geometric distortion only (EPI with 0.7 ms echo spacing), (c) signal loss from dephasing only (EPI with TE 30 ms). *In vivo* data from axial EPI acquisition at 3T, combined and viewed in the mid-sagittal plane: (d) 7 mm thick slice, (e) 3 mm thick slice.
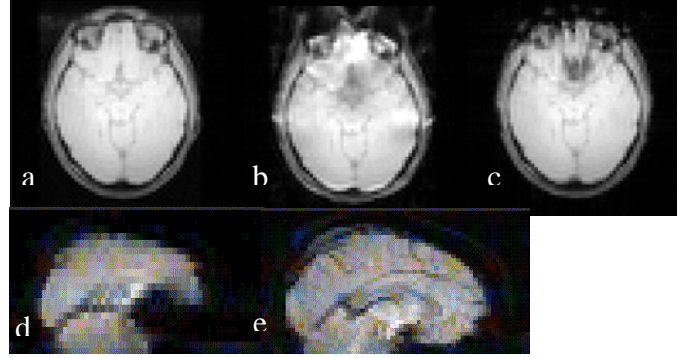
2. FIELD INHOMOGENEITY INDUCED DISTORTION

The BMS-induced distortion artifact depends on the data acquisition (k-space) trajectory and timing [3]. For a Cartesian acquisition (i.e. EPI), the BMS causes a significant geometric shift in image space along the slow-acquisition axis, *i.e.* the phase encode axis [4]. For a non-Cartesian acquisition, such as the spiral trajectory, the slow-acquisition axis is in the radial direction and blurring results in the radial direction [5].

The impact of field inhomogeneity on image distortion relies on the speed of acquisition of k-space for single-shot methods. For acquisitions that are not variable density, the bandwidth per pixel (BWPP) of the readout is equal to the inverse of the acquisition time. To calculate the geometric distortions or blurring that result from a certain level of field inhomogeneity, simply divide the value of the field map (in Hz) by the BWPP. For a single shot spiral acquisition with a readout duration (T_{ACQ}) of 20 ms, we can get the size of the blur in pixels in image space, δ, due to a field inhomogeneity (FI). For example, consider a field inhomogeneity of 100 Hz. For the acquisition above, the distortion of the point spread function in image space would be:

$$\delta = \frac{FI}{1/T_{ACQ}} = FI * T_{ACQ} = (100\,\text{Hz}) * (20\,\text{ms}) = 2\ \text{pixels}.$$

Many correction methods exist to compensate for the BMS-induced accrual of phase during the data readout and, hence, undo the resulting image distortions. Most methods start with a measurement of the distribution of the magnetic field resulting from BMS-induced inhomogeneities, *i.e.* form a field map (see field map estimation section). After estimating a field map, correction methods proceed to compensate for the distortions. For EPI trajectories, a common and effective way is to form a pixel-shift map that remaps the pixels to their original, undistorted locations [4, 6-8]. Several routines are available for correcting EPI data, including the Fugue utility in FSL (www.fmrib.ox.ac.uk/fsl/fugue).

Conjugate Phase
For spiral and other non-Cartesian acquisitions, the conjugate phase method is employed to undo the phase by multiplying the data by the conjugate of the phase accumulated; found from multiplying the field map by the timing during the acquisition [9-11]. The expression for the conjugate phase reconstruction can be given by

$$\hat{f}(\mathbf{r}) = \sum_{l=1}^{M} s(\mathbf{k}_l) \exp\left(i\omega(\mathbf{r})t_l\right) \exp\left(i2\pi\mathbf{k}_l \cdot \mathbf{r}\right),$$

where $s(\mathbf{k})$ is the signal in k-space at location $\mathbf{k}$, $\omega(\mathbf{r})$ is the field map in rad/sec at image position $\mathbf{r}$, t is the time at which sample $\mathbf{k}$ is acquired during the data readout, and M is the number of data samples in k-space. Note that the conjugate phase method performs well when the magnetic field inhomogeneity is

spatially smooth, which restricts significant overlap of point spread functions in adjacent voxels [9]. Normally, non-Cartesian data can be efficiently reconstructed using the gridding technique when field inhomogeneity is ignored [12]. However, due to the dependence of the field inhomogeneity term on both spatial position and time, gridding cannot be applied directly with the phase compensation. Instead, time-segmented [9] and frequency-segmented [10] versions of gridding are used.

Several other methods have been used to correct for magnetic field inhomogeneity. The SPHERE method uses a field map that is also measured in a BMS-distorted acquisition [13]. Another method utilizes an auto-focusing approach that attempts to refocus the point spread function [14, 15]. Recently, iterative reconstructions have been presented that model the phase accrual and result in more accurate image reconstructions in the vicinity of air/tissue interfaces [16-18].

Iterative Reconstruction
The iterative techniques begin with a forward model of the MRI signal that includes magnetic field inhomogeneity effects [16-18]. In [18], the image is modeled with voxels that are piece-wise constant, having a constant intensity and a constant field map offset due to magnetic susceptibility (Eqn 1).

$$s(t_m) = \Phi\big(\mathbf{k}(t_m)\big)\sum_{n=1}^{N} f(\mathbf{r}_n)\exp(-i2\pi\mathbf{k}_m \cdot \mathbf{r}_n)\exp(-i\omega(\mathbf{r}_n)t_m), \text{ for } m=1,...,M, \qquad (1)$$

where s(t) is the signal, f($\mathbf{r}$) is the image of the contrast-weighted spin density of the object, $\omega(\mathbf{r})$ is a measure of the magnetic field map (with a minus sign convention), N is the number of pixels, M is the number of data points in k-space, and $\Phi(\mathbf{k}(t))$ is the Fourier transform of the voxel indicator function, *i.e.* $sinc(\Delta_x k_x(t))*sinc(\Delta_y k_y(t))$, where (Δ_x,Δ_y) is the (x, y) dimension of the voxel. Using this signal model, a computationally efficient iterative reconstruction algorithm was developed that accurately reconstructs images corrected for BMS-induced geometric distortion and blurring [18, 19].

3. SUSCEPTIBILITY-INDUCED SIGNAL LOSS (SISL)

In addition to the image distortions, BOLD-based fMRI and other gradient echo imaging methods also suffer from susceptibility-induced signal loss (SISL) due to spin dephasing within a voxel, as the voxel size is usually quite large (~3-5 mm on a side), and the echo times (TE) are quite long (25-40 ms). Spin dephasing results from gradients in the magnetic field, such as near an air/tissue interface, causing protons within a voxel to experience slightly different magnetic field strengths across a voxel. The spins accumulate phase relative to their position within the voxel and signal cancellation occurs.

Several methods have been proposed to address signal cancellation: several acquisition-time interventions and one image reconstruction approach.
(1) **External/Internal Shims:** Improve shimming in orbitofrontal region by using devices such as a dielectric mouth insert [20-22], mouth shim coil [23], or dielectric foam [24]. This method requires subject-specific customization of hardware and may cause degradations in magnetic field uniformity elsewhere in the brain.
(2) **Tailored RF pulses**: Use RF pulses to apply a phase profile that counteracts the signal dephasing profile [25-27]. The recent development of transmit SENSE may make this more feasible [28]. However, more work needs to be done to address sensitivity to subject motion and real-time implementation demands, which limit application of this method.
(3) **Modifying pulse sequences**: Several modifications of pulse sequences have been developed to trade acquisition time for improved signal in high susceptibility areas. Note that both of the following approaches focus on gradients in the slice-select direction as this is usually the largest dimension. The simplest approach to mitigate SISL is to reduce the dimensions of the voxel in the slice-select direction [29-31]. An example from our own investigation of the gains in signal recovery by reducing slice thickness is shown in Figure 1(d, e). A second family of methods using an acquisition modification uses

an imbalanced slice-select gradient as compensation [32-35]. Several different unbalanced slice-select gradients are used to compensate for varying BMS-induced gradients within a slice. A single-shot methodology has been developed to measure two functionally weighted images simultaneously, one with a single z-compensating gradient and one without any compensation [36, 37]. Recently a sequence was presented that acquires spiral-in and spiral-out images with a Z-shim gradient between them to compensate for the signal loss [38, 39]. However, a different imbalanced gradient is needed to address different BMS-induced gradients within a slice, which may require additional acquisitions to fully compensate a slice.

(4) **Iterative reconstruction approach for signal loss correction and distortion correction**

The signal model (as shown in Eqn 1) models the object and the magnetic field distribution as *piece-wise constant*, so the magnetic field is assumed to be constant within a voxel. Further work has extended this signal model to include linear variation of the magnetic field across a voxel, enabling a *piece-wise linear* approximation within a voxel [40, 41]. The *piece-wise linear* model allows for an image-based recovery of signal loss due to BMS-induced dephasing. The piece-wise linear expansion will be used for the field map, allowing for weighting the phase accrual across a voxel. However, since we are constructing an image to be displayed as constant-intensity pixels, the piece-wise constant expansion is kept for the object. With the piece-wise linear model for the magnetic field map only, the signal model becomes:

$$s(t_m) = \sum_{n=1}^{N} \Phi\left(k_x(t_m), k_y(t_m), X_n, Y_n, Z_n\right) f(\mathbf{r}_n) \exp(-i2\pi\mathbf{k}_m \cdot \mathbf{r}_n) \exp(-i\omega(\mathbf{r}_n)t_m), \text{ for } m = 1,...,M \qquad (2)$$

where $\Phi(k_x(t), k_y(t), X_n, Y_n, Z_n) = sinc(\Delta_x k_x(t) + X_n t/2\pi) * sinc(\Delta_y k_y(t) + Y_n t/2\pi) * sinc(Z_n t/2\pi)$, with (X_n, Y_n, Z_n) denoting the linear slopes in the magnetic field distribution in (x,y,z) over voxel n.

With the signal model given in Equation (2) along with the magnetic field map and the gradients of that field map, we can construct an iterative image reconstruction algorithm that attempts to estimate the image required to create the observed signal. An example fMRI data set was acquired with a 4 mm slice thickness and a 64x64 matrix size. In addition to the fMRI acquisition, a multi-echo field map was acquired with a 2 mm slice thickness with adjacent slices matching the slice prescription of the 4 mm acquisition. The multi-echo acquisition was used to estimate both the field map values and the gradients, which were calculated as numerical gradients of the higher resolution field map. Figure 2 panel (d) demonstrates the performance of the image reconstruction approach: the region of BMS-induced signal loss is much reduced for piece-wise linear field map [40].

Figure 2. EPI data set reconstructed with varying levels of correction for BMS-induced distortions and signal loss. (a) Reference anatomical image, (b) uncorrected fMRI image with BMS-induced distortion and signal loss, (c) iterative reconstruction with piece-wise constant field map showing reduced BMS-induced **geometric distortions**, (d) iterative reconstruction with piece-wise linear field map showing reduction of **BMS-induced signal loss** along with further reduction of image distortion.
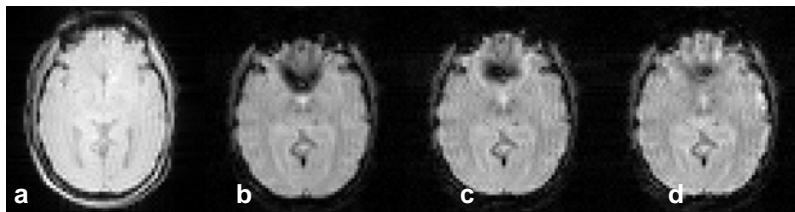
4. ROLE OF PARALLEL IMAGING IN REDUCING BMS DISTORTIONS

In addition to devices reshaping the magnetic field and sequence modifications for signal recovery, a major advance in MRI data acquisition has been the use of parallel receiver networks. Instead of using a single volume receive coil, arrays of receiver coils are arranged around the object with each receiver coil being sensitive to a subset of the object. By taking advantage of the localized sensitivity of the receiver coils, several methods have been developed to acquire data more quickly by subsampling the data space.

Full field-of-view, unaliased images are reconstructed by considering the spatial sensitivity of the individual receiver coils. By reconstructing images from subsampled k-space, data acquisition time for a single image is shorter. The reduction in data readout time results in less BMS-induced distortions in the image. Parallel image reconstruction can occur in image space as in SENSE [42], k-space as in GRAPPA [43], or other methods [44].

5. ESTIMATION OF MAGNETIC FIELD INHOMOGENEITY MAPS

As mentioned above, image reconstruction approaches for correction of BMS-induced distortions and dephasing require measurements of the magnetic field inhomogeneity. Traditionally, magnetic field inhomogeneity maps are measured prior to or subsequent to functional MRI acquisitions using two different echo times [45]. The expression for the field map (FM) in rad/sec is,

$$FM = -\frac{\sphericalangle I(TE + \Delta t) - \sphericalangle I(TE)}{\Delta t}$$

where $I(TE+\Delta t)$ is the image acquired at an echo time of $TE+\Delta t$ and $I(TE)$ is the image acquired at echo time TE. See Figure 3 for an example phase map at a short echo time (1.5 ms).

Traditionally, the magnetic field is measured through a static procedure and does not reflect changes due to subject motion. However, the field distribution around air/tissue interfaces depends on the geometry of those interfaces and their orientation with respect to the main magnetic field [20, 46]. Subject movement can cause nonlinear changes in this field distribution and its gradients [3]. In order to accurately correct for dynamic BMS effects, the magnetic field distribution must be measured dynamically and in register with the image acquisition. This field map may be measured through multiple echo EPI [47], however, the resulting field maps would themselves suffer from BMS-induced distortions. Recently, several groups have proposed methods to jointly estimate the field-corrected image and the distorting magnetic field map from an extended acquisition [17, 48, 49].

## 6. IN-PLANE FIRST ORDER EFFECTS OF FIELD INHOMOGENEITY

In the discussion above, two susceptibility effects were discussed: the zeroth order effects of BMS-induced image distortions and the first-order through-plane effect of BMS-induced signal loss. Besides these effects, gradients in the magnetic field inhomogeneity can cause additional effects in the reconstructed images. In [50], a method was presented to analyze the changes in point spread function that result from both zeroth and first order effects of the magnetic field inhomogeneity in a spiral acquisition. Without loss of generality, we can consider the effect of a gradient in the magnetic field inhomogeneity in the x-direction. This effect is in addition to the effects given in Equation 1. The additional gradient in a voxel due to the magnetic susceptibility creates an effective k-space trajectory that deviates from the intended imaging trajectory. The effective trajectory can be found by integrating the net gradient, which is given by,

$$G_x^{TOT}(\mathbf{r}) = G_x^{IMAGING} + G_x^{SUSC}(\mathbf{r})$$

where $G_x^{TOT}(\mathbf{r})$ is the net gradient in the voxel at position $\mathbf{r}$, $G_x^{IMAGING}$ is the applied imaging gradient in the x-direction (same for every voxel), and $G_x^{SUSC}(\mathbf{r})$ is the gradient in the magnetic susceptibility induced field map in the x-direction at voxel position $\mathbf{r}$. This results in a k-space trajectory that is spatially dependent. The local shifts in the k-space trajectory can cause difficulties in properly compensating the sample density for reconstruction and can result in echo time shifts for different voxels in an imaging experiment. Additionally, the shifts may result in signal loss if the k-space trajectory is shifted far enough that the center of k-space is not sampled [51].

Several studies have examined these effects on the reconstructed image. In [51], a maximum echo time for gradient echo experiments was determined to achieve sufficient sampling of the signal intensity in a voxel with a given gradient distribution. In [52], the stretched and compressed spiral k-space trajectories resulting from the susceptibility gradients were included in calculations of sample density compensation. It was found that much of the residual pile-up artifact that persists after conjugate phase reconstruction can be corrected by taking into account the sample density function of the net k-space trajectory at the origin. Finally, due to the echo time dependence of the BOLD signal, the spatially dependent shifts in echo time can also effect sensitivity in fMRI studies in regions with high gradients in the magnetic field inhomogeneity distribution [53].

Figure 3: Phase map from 16-shot 3D GRE spiral (1.5 ms TE), sagittal and axial views.
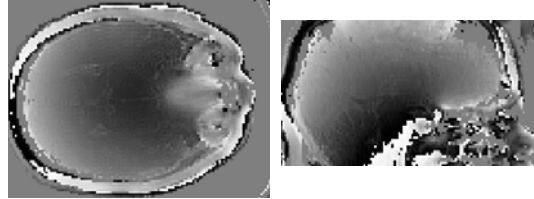
7. REFERENCES

1.   Lauterbur, P.C. Image formation by induced local interactions: Examples employing nuclear magnetic resonance. *Nature*, 1973. 242: p. 190-191.
2.   Yoder, D.A., Y. Zhao, C.B. Paschal, and J.M. Fitzpatrick. MRI simulator with object-specific field map calculations. *Magn Reson Imaging*, 2004. 22(3): p. 315-328.
3.   Jezzard, P. and S. Clare. Sources of distortion in functional MRI data. *Human brain mapping*, 1999. 8(2-3): p. 80-5.
4.   Sekihara, K., M. Kuroda, and H. Kohno. Image restoration from non-uniform magnetic field influence for direct Fourier NMR imaging. *Physics in Medicine and Biology*, 1984. 29(1): p. 15-24.
5.   Yudilevich, E. and H. Stark. Spiral sampling in magnetic resonance imaging - the effect of inhomogeneities. *IEEE Trans Med Imaging*, 1987. 6(4): p. 337-345.
6.   Sumanaweera, T.S., G.H. Glover, T.O. Binford, and J.R. Adler. MR susceptibility misregistration correction. *IEEE Trans Med Imaging*, 1993. 12(2): p. 251-259.
7.   Jezzard, P. and R.S. Balaban. Correction for geometric distortion in echo planar images from B0 field variations. *Magn Reson Med*, 1995. 34: p. 65-73.
8.   Reber, P.J., E.C. Wong, R.B. Buxton, and L.R. Frank. Correction of off resonance-related distortion in echo-planar imaging using EPI-based field maps. *Magn Reson Med*, 1998. 39: p. 328-330.
9.   Noll, D.C., C.H. Meyer, J.M. Pauly, D.G. Nishimura, and A. Macovski. A homogeneity correction method for magnetic resonance imaging with time-varying gradients. *IEEE Trans Med Imaging*, 1991. 10(4): p. 629-637.
10.   Man, L.C., J.M. Pauly, and A. Macovski. Multifrequency interpolation for fast off-resonance correction. *Magn Reson Med*, 1997. 37: p. 785-792.
11.   Schomberg, H. Off-resonance correction of MR images. *IEEE Trans Med Imaging*, 1999. 18(6): p. 481-495.
12.   Jackson, J.I., C.H. Meyer, D.G. Nishimura, and A. Macovski. Selection of a convolution function for Fourier inversion using gridding. *IEEE Trans Med Imaging*, 1991. 10(3): p. 473-478.
13.   Kadah, Y.M. and X. Hu. Simulated phase evolution rewinding (SPHERE): A technique for reducing B0 inhomogeneity effects in MR images. *Magn Reson Med*, 1997. 38: p. 615-627.
14.   Noll, D.C., J.M. Pauly, C.H. Meyer, D.G. Nishimura, and A. Macovski. Deblurring for non-2D Fourier transform magnetic resonance imaging. *Magn Reson Med*, 1992. 25: p. 319-333.

15. Man, L.C., J.M. Pauly, and A. Macovski. Improved automatic off-resonance correction without a field map in spiral imaging. *Magn Reson Med*, 1997. 37: p. 906-913.

16. Harshbarger, T.B. and D.B. Twieg. Iterative reconstruction of single-shot spiral MRI with off resonance. *IEEE Trans Med Imaging*, 1999. 18(3): p. 196-205.

17. Twieg, D.B. Parsing local signal evolution directly from a single-shot MRI signal: a new approach for fMRI. *Magn Reson Med*, 2003. 50(5): p. 1043-1052.

18. Sutton, B.P., D.C. Noll, and J.A. Fessler. Fast, iterative, field-corrected image reconstruction for MRI. *IEEE Trans Med Imaging*, 2003. 22(2): p. 178-188.

19. Fessler, J.A. Penalized weighted least-squares image reconstruction for positron emission tomography. *IEEE Trans Med Imaging*, 1994. 13(2): p. 290-300.

20. Wilson, J.L. and P. Jezzard. Utilization of an intra-oral diamagnetic passive shim in functional MRI of the inferior frontal cortex. *Magn Reson Med*, 2003. 50(5): p. 1089-1094.

21. Wilson, J.L., M. Jenkinson, and P. Jezzard. Protocol to determine the optimal intraoral passive shim for minimisation of susceptibility artifact in human inferior frontal cortex. *NeuroImage*, 2003. 19(4): p. 1802-1811.

22. Cusack, R., B. Russell, S.M. Cox, C. De Panfilis, C. Schwarzbauer, and R. Ansorge. An evaluation of the use of passive shimming to improve frontal sensitivity in fMRI. *NeuroImage*, 2005. 24(1): p. 82-91.

23. Hsu, J.J. and G.H. Glover. Mitigation of susceptibility-induced signal loss in neuroimaging using localized shim coils. *Magn Reson Med*, 2005. 53(2): p. 243-248.

24. Shah, R.N., A.C.M. Chen, L.Y. Li, B.A. Hargreaves, and S.M. Conolly. *An improved pyrolytic graphite foam for tissue susceptibility matching in MRI*, in *Proc. Intl. Soc. of Mag. Reson. Med. 15*. 2007. p. 3434.

25. Ro, Y.M. and Z.H. Cho. A new frontier of blood imaging using susceptibility effect and tailored RF pulses. *Magn Reson Med*, 1992. 28(2): p. 237-248.

26. Stenger, V.A., F.E. Boada, and D.C. Noll. Three-dimensional tailored RF pulses for the reduction of susceptibility artifacts in T(*)(2)-weighted functional MRI. *Magn Reson Med*, 2000. 44(4): p. 525-531.

27. Stenger, V.A., F.E. Boada, and D.C. Noll. Multishot 3D slice-select tailored RF pulses for MRI. *Magn Reson Med*, 2002. 48(1): p. 157-165.

28. Katscher, U., P. Bornert, C. Leussler, and J.S. van den Brink. Transmit SENSE. *Magn Reson Med*, 2003. 49: p. 144-150.

29. Merboldt, K.D., J. Finsterbusch, and J. Frahm. Reducing inhomogeneity artifacts in functional MRI of human brain activation-thin sections vs gradient compensation. *Journal of Magn Reson*, 2000. 145(2): p. 184-191.

30. Wadghiri, Y.Z., G. Johnson, and D.H. Turnbull. Sensitivity and performance time in MRI dephasing artifact reduction methods. *Magn Reson Med*, 2001. 45(3): p. 470-476.

31. Bellgowan, P.S., P.A. Bandettini, P. van Gelderen, A. Martin, and J. Bodurka. Improved BOLD detection in the medial temporal region using parallel imaging and voxel volume reduction. *NeuroImage*, 2006. 29(4): p. 1244-1251.

32. Frahm, J., K.D. Merboldt, and W. Hanicke. Direct FLASH MR imaging of magnetic field inhomogeneities by gradient compensation. *Magn Reson Med*, 1988. 6(4): p. 474-480.

33. Glover, G.H. 3D z-shim method for reduction of susceptibility effects in BOLD fMRI. *Magn Reson Med*, 1999. 42(2): p. 290-299.

34. Yang, Q.X., B.J. Dardzinski, S. Li, P.J. Eslinger, and M.B. Smith. Multi-gradient echo with susceptibility inhomogeneity compensation (MGESIC): demonstration of fMRI in the olfactory cortex at 3.0 T. *Magn Reson Med*, 1997. 37(3): p. 331-335.

35. Yang, Q.X., G.D. Williams, R.J. Demeure, T.J. Mosher, and M.B. Smith. Removal of local field gradient artifacts in T2*-weighted images at high fields by gradient-echo slice excitation profile imaging. *Magn Reson Med*, 1998. 39(3): p. 402-409.

36.   Heberlein, K.A. and X. Hu. Simultaneous acquisition of gradient-echo and asymmetric spin-echo for single-shot z-shim: Z-SAGA. *Magn Reson Med*, 2004. 51(1): p. 212-216.

37.   Song, A.W. Single-shot EPI with signal recovery from the susceptibility-induced losses. *Magn Reson Med*, 2001. 46(2): p. 407-411.

38.   Guo, H. and A.W. Song. Single-shot spiral image acquisition with embedded z-shimming for susceptibility signal recovery. *J Magn Reson Imaging*, 2003. 18(3): p. 389-95.

39.   Truong, T.K. and A.W. Song. Single-shot dual-z-shimmed sensitivity-encoded spiral-in/out imaging for functional MRI with reduced susceptibility artifacts. *Magn Reson Med*, 2008. 59(1): p. 221-7.

40.   Sutton, B.P., D.C. Noll, and J.A. Fessler. *Compensating for within-voxel susceptibility gradients in BOLD fMRI*, in *12th Soc. Magn. Reson. Med*. 2004. p. 349.

41.   Liu, G. and S. Ogawa. EPI image reconstruction with correction of distortion and signal losses. *J Magn Reson Imaging*, 2006. 24(3): p. 683-9.

42.   Pruessmann, K.P., M. Weiger, M.B. Scheidegger, and P. Boesiger. SENSE: Sensitivity encoding for fast MRI. *Magn Reson Med*, 1999. 42: p. 952-962.

43.   Griswold, M.A., P.M. Jakob, R.M. Heidemann, M. Nittka, V. Jellus, J. Wang, B. Kiefer, and A. Haase. Generalized autocalibrating partially parallel acquisitions (GRAPPA). *Magn Reson Med*, 2002. 47: p. 1202-1210.

44.   Blaimer, M., F. Breuer, M. Mueller, R.M. Heidemann, M.A. Griswold, and P.M. Jakob. SMASH, SENSE, PILS, GRAPPA: how to choose the optimal method. *Top Magn Reson Imaging*, 2004. 15(4): p. 223-36.

45.   Schneider, E. and G. Glover. Rapid in vivo proton shimming. *Magn Reson Med*, 1991. 18: p. 335-347.

46.   Truong, T.K., B.D. Clymer, D.W. Chakeres, and P. Schmalbrock. Three-dimensional numerical simulations of susceptibility-induced magnetic field inhomogeneities in the human head. *Magn Reson Imaging*, 2002. 20(10): p. 759-770.

47.   Hutton, C., A. Bork, O. Josephs, R. Deichmann, J. Ashburner, and R. Turner. Image distortion correction in fMRI: A quantitative evaluation. *NeuroImage*, 2002. 16(1): p. 217-40.

48.   Sutton, B.P., D.C. Noll, and J.A. Fessler. Dynamic field map estimation using a spiral-in/spiral-out acquisition. *Magn Reson Med*, 2004. 51: p. 1194-1204.

49.   Priest, A.N., E. De Vita, D.L. Thomas, and R.J. Ordidge. EPI distortion correction from a simultaneously acquired distortion map using TRAIL. *J Magn Reson Imaging*, 2006. 23(4): p. 597-603.

50.   Maeda, A., K. Sano, and T. Yokoyama. Reconstruction by weighted correlation for MRI with time-varying gradients. *IEEE Trans Med Imaging*, 1988. 7(1): p. 26-31.

51.   Reichenbach, J.R., R. Venkatesan, D.A. Yablonskiy, M.R. Thompson, S. Lai, and E.M. Haacke. Theory and application of static field inhomogeneity effects in gradient-echo imaging. *J Magn Reson Imaging*, 1997. 7(2): p. 266-79.

52.   Noll, D.C., J.A. Fessler, and B.P. Sutton. Conjugate phase MRI reconstruction with spatially variant sample density correction. *IEEE Trans Med Imaging*, 2005. 24(3): p. 325-36.

53.   Zhuo, Y. and B.P. Sutton. *Echo time shift analysis based on field-inhomogeneity gradients in BOLD fMRI*, in *17th Intl Soc Magn Reson Med*. 2009. p. Submitted.